Journal of
Materials Chemistry A

ROYAL SOCIETY
OF CHEMISTRY

PAPER

View Article Online
View Journal | View Issue

Check for updates

Cite this: *J. Mater. Chem. A*, 2024, **12**, 17169

Deciphering the role of aromatic cations in electrochemical CO_2 reduction: interfacial ion assembly governs reaction pathways†

Wenxiao Guo, Beichen Liu, Seth R. Anderson, Samuel G. Johnstone and Matthew A. Gebbie *

The accumulation of ions at electrochemical interfaces governs the local chemical environment, which in turn determines the reaction pathways and rates of electrocatalytic processes, including electrochemical CO_2 reduction. Imidazolium cations have been shown to promote CO_2 reduction in nonaqueous electrolytes, where multiple mechanisms have been proposed for how imidazolium facilitates CO_2 reduction. However, many puzzles persist surrounding how imidazolium cations modify local chemical environments at electrochemical interfaces during CO_2 reduction. Dialkylimidazolium cations are multifunctional species that interact with adsorbed $CO_2^{\bullet-}$ while also donating protons and forming carbene-mediated coordination complexes. In this work, we exploit the combination of independent proton donor $[Et_3NH]Cl$ and aprotic imidazolium cations, namely 1-ethyl-2,3-dimethylimidazolium ($[EMMIm]^+$) and 1-ethyl-2,3,4,5-tetramethylimidazolium ($[EM_4Im]^+$) to further illuminate how imidazolium cations promote selective CO_2 electrochemical reduction. Our data indicates that the presence of an aromatic, planar delocalized charge region on imidazolium rings plays an essential role in stabilizing $CO_2^{\bullet-}$ to promote electrocatalytic reduction. Kinetic and steady-state electrochemical analysis demonstrates that ring substituents of $[EMMIm]^+$ additionally tune local chemical environments to impact the rate and product distribution of CO_2 reduction by limiting the transport of proton donors. Further, we leverage surface-enhanced Raman scattering in the presence of a molecular probe of local electric fields to illustrate that the unique interface-tuning properties of $[EMMIm]^+$ stem from potential-driven assembly at cathodes. Our study highlights how imidazolium substituents can be tuned to regulate interfacial electrochemical environments and illustrates the importance of balancing $CO_2^{\bullet-}$ stabilization and proton transport in sustaining steady-state electrochemical CO_2 reduction with high rate and selectivity. More broadly, our results suggest that aromatic cations promote electrochemical CO_2 reduction *via* a distinct "π^+–anion" interaction that appears to be the electrostatic analog of the more commonly investigated "cation–π" interaction, which drives self-assembly in proteins and many other biological systems.

Received 26th April 2024
Accepted 11th June 2024

DOI: 10.1039/d4ta02903h

rsc.li/materials-a

Introduction

Electrochemical CO_2 reduction to chemicals and fuels could provide one avenue towards reducing carbon emissions associated with energy consumption and provide sustainable alternatives for fossil fuels in applications where decarbonization is difficult.[1–3] Electrochemical CO_2 reduction involves multiple proton-coupled electron transfers from electrodes to CO_2, which usually yields a mixture of products. For instance, two-electron reduction of CO_2 can lead to both CO and formate (or formic acid), and more complex mixtures arise when more reduced products are generated, such as methane, methanol, and multi-carbon products. The reduction of water always takes place in parallel, generating hydrogen as a competing side product.

The production of mixtures adds substantial energy and hardware costs for product separation.[4,5] Therefore, it is desirable to develop methods to selectively direct CO_2 reduction towards targeted pathways, leading to controlled product selectivity. Current theories indicate that one critical aspect determining the reaction selectivity in CO_2 reduction is the relative adsorption energy of intermediates involved in the rate-determining step of different pathways, as the formation of more strongly adsorbed intermediates provides a larger thermodynamic driving force for the conversion.[6,7]

As a result, various strategies are being developed to tune the adsorption energy of relevant intermediates. One major and

---

Department of Chemical and Biological Engineering, University of Wisconsin–Madison, Madison, Wisconsin 53706, USA. E-mail: gebbie@wisc.edu

† Electronic supplementary information (ESI) available. See DOI: https://doi.org/10.1039/d4ta02903h

conventional category of strategies is engineering electrode surface structures and electronic properties.[3,8–12] For example, increasing the number of low-coordinating sites and grain boundaries on electrode surfaces,[10,13] alloying of metal electrodes,[11,12] and developing new heterogeneous catalytic materials with tunable active sites[14–16] are all demonstrated to increase the rate and selectivity of CO_2 reduction in aqueous solutions by tuning the adsorption energy of key intermediates.

Notably, electrochemical reactions occur at the electrode–electrolyte interface, meaning that electrodes comprise only one-half of an electrocatalytic interface. Indeed, there has been a resurgence in interest in studying how electrolyte properties also influence electrocatalytic reactions,[17–19] and many recent studies have shown that the properties of electrolytes can play at least an equally important role as electrodes in controlling reaction activity and selectivity. For instance, strategies such as increasing electrolyte pH,[20–23] changing the identity of supporting cations,[24–26] and decreasing water activity by increasing electrolyte concentration have been employed to enhance both the overall CO_2 conversion selectivity *versus* water reduction and the selective generation of multi-carbon products.[27]

While electrode engineering primarily influences reaction pathways through changes in adsorbate binding energies, electrolytes can influence the electrocatalytic process through multiple mechanisms, including changes in interfacial electric field gradients, alterations to proton transport, and modification of thermodynamic activity of both products and reactants.[7,24–29] This multidimensional control enables distinct opportunities for studying and understanding electrochemical CO_2 reduction and promises to reveal new strategies for impacting other emerging electrocatalytic reactions, such as nitrate reduction and selective C–N bond formation.

Designing and modifying electrolytes based on ionic liquids is an especially promising strategy for electrolyte engineering. Ionic liquids are salts consisting of weakly coordinating organic cations and anions and are defined as exhibiting a melting point below 100 °C for pure salt. Ionic liquids have highly tunable ion structures, high intrinsic conductivity, wide electrochemical windows, and can be designed to be proton donors or acceptors.[30–33] These properties provide many avenues for using ionic liquids as co-catalytic promoters in electrocatalysis. Further, ionic liquids are soluble in nonaqueous and aprotic solvents, circumventing competing water reduction and providing opportunities for detailed mechanistic study of proton-coupled electron transfers in electrochemical CO_2 reduction by introducing external proton donors.

To date, imidazolium-based ionic liquids have been the most widely used ionic liquid cation in electrochemical CO_2 reduction.[34–38] Electrolytes based on dialkylimidazolium ionic liquids, such as 1-ethyl-3-methylimidazolium tetrafluoroborate ($[EMIm][BF_4]$), have been repeatedly demonstrated to significantly lower the overpotential of electrochemical CO_2 reduction.[38–41] Many prior studies attributed the catalytic activity of dialkylimidazolium to the stabilization of adsorbed CO_2 by protons at C4/5 positions *via* hydrogen bonds.[40–42] Further, recent studies have proven that the proton at the C2 position of dialkylimidazolium can act as proton donors with high activity during electrochemical CO_2 reduction.[43,44]

While there is a general agreement supporting the importance of both proton activity and transition state stabilization effects in dialkylimidazolium ionic liquids, the relative importance of these two functions in imidazolium ionic liquids remains unclear. Further, there are apparent discrepancies regarding whether methylation of the C2 of imidazolium rings to block proton transfer promotes or inhibits CO_2 reduction.[45] For example, voltammetry studies of reaction kinetics suggest that ring methylation promotes selective CO_2 reduction by preventing the formation of a carbene–CO_2 adduct that inhibits CO_2 reduction.[39,40] Yet, steady-state reaction rate studies suggest that C2 methylation instead inhibits CO_2 reduction through the formation of carbonate imidazolium precipitates that block electron transfer.[38,44] Therefore, to accurately understand the function of and more efficiently use imidazolium in electrochemical CO_2 reduction, it is necessary to deconvolute their proton-donating and intermediate-stabilizing capabilities.

In this study, we systematically investigated the role of imidazolium without proton-donating capability in electrochemical CO_2 reduction by instead using an alternative organic proton donor as the proton source for CO_2 electroreduction. We compare the rate and product distribution of electrochemical CO_2 reduction on polycrystalline Ag disk electrodes in acetonitrile electrolytes of 1-ethyl-2,3-dimethylimidazolium tetrafluoroborate ($[EMMIm][BF_4]$), 1-ethyl-2,3,4,5-tetramethylimidazolium tetrafluoroborate ($[EM_4Im][BF_4]$), and tetrabutylammonium tetrafluoroborate ($[TBA][BF_4]$) without the imidazolium ring in the presence of the cationic proton donor triethylammonium chloride ($[Et_3NH]Cl$).

We first demonstrate that the imidazolium ring is the core functional group involved in stabilizing CO_2 by comparing the selectivity and activity of electrochemical CO_2 reductions in $[EMMIm][BF_4]$, $[EM_4Im][BF_4]$, and $[TBA][BF_4]$ electrolytes. Further, by combining kinetic analysis and studies of binary mixtures of imidazolium-based ionic liquids and $[TBA][BF_4]$, we unravel the role of C4/5-H in enhancing the surface activity of $[EMMIm]^+$ and suppressing proton transfer. Interestingly, we found that while such high surface activity of $[EMMIm]^+$ and suppressed proton transfer might contribute to higher instant electrochemical CO_2 reduction rate and selectivity towards CO, they largely compromise the steady-state CO_2 reduction rate, likely due to the rapid depletion of protons at electrochemical interfaces and the consequential discontinuation of proton-coupled electron transfer to CO_2.

Taken together, our study provides a new understanding of the roles played by aprotic imidazolium cations in electrochemical CO_2 reduction. Our findings further highlight the necessity of balancing the suppression of proton reduction and the promotion of proton-coupled electron transfers in designing electrolytes for CO_2 upgrading systems.

Results and discussion

To date, several mechanisms have been proposed for how imidazolium-based ionic liquids promote CO_2 reduction. One dominating hypothesis is that the stabilization of one-electron reduced $CO_2^{\bullet -}$ intermediate adsorbed on the electrode surface by protons at C4/5 positions (C4/5-H) through hydrogen bonds is critical for promoting selective CO_2 reduction.[41,42] Alternatively, stabilizing electrochemical interactions between the positive aromatic ring and anionic $CO_2^{\bullet -}$ has also been explored as a mechanism for how imidazolium cations promoted CO_2 reduction, but this mechanism has received less attention than those invoking hydrogen bond interactions.[46] Interestingly, many studies of hydrogen bonding stabilization have focused on dialkylimidazolium cations, such as 1-ethyl-3-methyl imidazolium ($[EMIm]^+$), with free protons at the C2 position (C2-H).[40,41] While the C2-H has low acidity and was assumed to only participate in CO_2 reduction by forming hydrogen bonds with $CO_2^{\bullet -}$, recent studies establish that C2-H of imidazolium can act as a proton donor during CO_2 reduction, which convolutes with the proposed roles of ring protons and the aromatic ring.[43,44]

To unambiguously investigate the role of imidazolium cations in CO_2 reduction beyond donating C2-H as the proton source, we analyze the reaction rate and product distribution in acetonitrile electrolytes of aprotic imidazolium ionic liquids, namely $[EM_4Im][BF_4]$ and $[EMMIm][BF_4]$, where protons are instead sourced from a tertiary ammonium cation. We selected these materials as $[EM_4Im]^+$ only possesses the imidazolium aromatic ring with no ring protons, while $[EMMIm]^+$ has both the aromatic ring and C4/5-Hs. All ionic liquids exhibit good electrochemical stability (Fig. S2†). We compare CO_2 reduction performance in these electrolytes with that from electrolyte [TBA] $[BF_4]$, which has neither ring protons nor aromatic rings, thus serving as an "inert" control for $[EM_4Im]^+$ and $[EMMIm]^+$. Further, $[Et_3NH]Cl$ was added to all electrolytes as the independent proton donor to circumvent the extraction of proton from water absorbed by the electrolyte, which were demonstrated to release hydroxide that caused bicarbonate precipitation-induced passivation of electrochemical interfaces.[38,44,47]

Fig. 1 shows cyclic voltammetry measurements collected from electrolytes of the three ionic liquids at concentrations ranging from 0.025 M to 0.7 M on commercial polycrystalline Ag disk electrodes at a scan rate of 100 mV/s. The electrolytes were saturated with CO_2, and 0.05 M $[Et_3NH]Cl$ was added to all electrolytes as the proton source. In $[TBA][BF_4]$ electrolytes, the maximum current density in each voltammetry scan shows a nonmonotonic dependence on the $[TBA][BF_4]$ concentration, and the highest current density was achieved at 0.2 M $[TBA][BF]_4$ (Fig. 1A). Further increasing the concentration over 0.2 M leads to decreases in current density, which is likely due to the smaller relative concentration of proton donor $[Et_3NH]^+$ in view of the similar trend under Ar purging condition (Fig. S3†).

In contrast to $[TBA][BF_4]$, the current density in $[EM_4Im][BF_4]$ and $[EMMIm][BF_4]$ monotonically increases with increased ionic liquid concentration at corresponding applied potentials, indicating that the facilitation of CO_2 reduction brought by imidazolium cations surpasses effects brought by lower relative concentration of proton donors on the time scale of voltammetry scans. More interestingly, $[EMMIm][BF_4]$ electrolytes facilitate much higher current density than both $[TBA][BF_4]$ and $[EM_4Im][BF_4]$ electrolytes at all concentrations above 0.1 M, which seems to align with prior studies concluding that $[EMMIm]^+$ is the most effective imidazolium cation to facilitate CO_2 reduction.[39,40]

To further understand reaction pathways in electrolytes composed of the three ionic liquids, we conducted chronoamperometry and analyzed product distributions of CO_2 reduction in $[TBA][BF_4]$, $[EM_4Im][BF_4]$, and $[EMMIm][BF_4]$ electrolytes at concentrations ranging from 0 to 0.7 M (Fig. 2) at −2.5 V *vs.* Ag/Ag$^+$. For all three electrolytes, the total current density first increases with ionic liquid concentration and then tapers ($[EM_4Im][BF_4]$) or slightly decreases ($[TBA][BF_4]$ and $[EMMIm][BF_4]$) after ionic liquid concentration exceeds 0.2 M, likely due to the decrease in the relative concentration of proton donor $[Et_3NH]^+$.

In $[TBA][BF_4]$ electrolytes at all concentrations, H_2 from the direct reduction of $[Et_3NH]^+$ is the dominant product. In contrast, two-electron reduction of CO_2 to either formate or CO becomes the favorable pathway in both $[EM_4Im][BF_4]$ and $[EMMIm][BF_4]$ electrolytes at concentrations higher than 0.1 M, with CO as the more dominant product. This result strongly indicates that the imidazolium ring, with or without ring

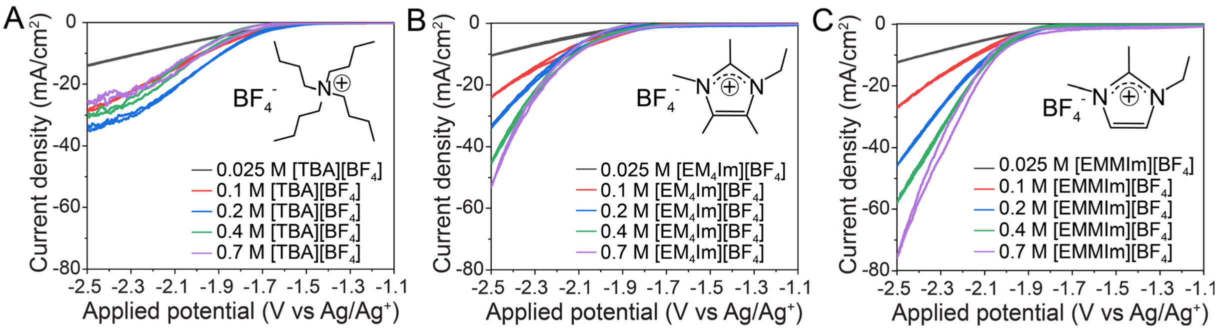

Fig. 1 Cyclic voltammetry in CO_2-purged (A) $[TBA][BF_4]$, (B) $[EM_4Im][BF_4]$, and (C) $[EMMIm][BF_4]$ electrolytes at concentrations ranging from 0.025 M to 0.7 M. All electrolytes contained 0.05 M $[Et_3NH]Cl$ as the proton donor and were scanned at 100 mV/s. At concentrations higher than 0.2 M, both $[EM_4Im][BF_4]$ and $[EMMIm][BF_4]$ electrolytes give higher current density than $[TBA][BF_4]$ electrolytes at matching concentrations, while the highest current density was achieved in $[EMMIm][BF_4]$ electrolytes. These comparisons suggest the critical role of imidazolium ring structure in facilitating CO_2 reduction.

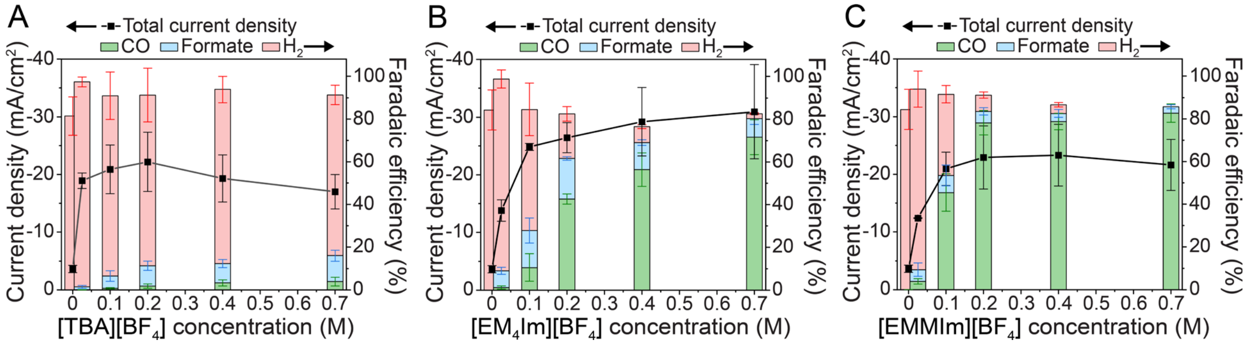

Fig. 2 Total current density and product selectivity of electrochemical CO_2 reduction in (A) [TBA][BF_4], (B) [EM_4Im][BF_4], and (C) [EMMIm][BF_4] electrolytes at different concentrations with 0.05 M [Et_3NH]Cl as the proton donor. For each trial, the potential was held at −2.5 V *vs.* Ag/Ag^+ for 65 min under stirring (600 rpm) and CO_2 purging. Direct reduction of $[Et_3NH]^+$ to H_2 is the dominant reaction pathway in [TBA][BF_4] electrolytes. In contrast, both [EM_4Im][BF_4] and [EMMIm][BF_4] electrolytes facilitate CO_2 reduction at concentrations higher than 0.1 M. [EM_4Im][BF_4] electrolytes exhibit higher steady-state total current density and thus overall CO_2 conversion rate by producing both formate and CO, while [EMMIm][BF_4] electrolytes yield lower steady-state total current density but higher selectivity towards CO.

protons, is the key functional group to stabilize CO_2 and facilitate CO_2 reduction.

Prior computational studies indicate that the +1 charge of tetraalkylammonium is mainly distributed on eight randomly orientated methylene hydrogens closest to the center N atom.[48] In comparison, the +1 charge of the imidazolium ring in $[EMMIm]^+$ is co-planarly distributed on C2, C4-H, and C5-H atoms, with the C2 atom carrying the highest partial positive charge.[49,50] While rare theoretical studies are found for $[EM_4Im]^+$, an analog to the comparison between $[EMMIm]^+$ and $[EMIm]^+$ that distributes positive charge on C2, C2-H, C4-H, and C5-H atoms suggests the distribution of the positive charge on C2, C4, and C5 atoms in $[EM_4Im]^+$, with the C2 atom still carrying the highest partial positive charge.[49,50]

Additionally, spectroscopic studies and density functional theory of cation–anion interaction energetics and configurations of gas phase ion pair interactions and molecular dynamics simulations performed on neat $[EMMIm]^+$-derived ionic liquids indicate that anions mainly interact with $[EMMIm]^+$ directly above or below the C2 position, which is the site of maximum partial positive charge density.[50–52] Thus, combined with our CO_2 reduction results, we conclude that the co-planar distribution of positive charge centered on the C2 position of imidazolium is the key to stabilizing adsorbed $CO_2^{\bullet-}$ and facilitating the reduction of CO_2 to CO. This "π–anion interaction" between aromatic cations and adsorbed anionic species is an analog to the widely studied cation–π interaction that drives self-assembly of large molecules in biological systems and has important implications in designing electrolytes for electrocatalysis.[53,54]

Despite the shared core ring structure, [EM_4Im][BF_4] and [EMMIm][BF_4] electrolytes still behave distinctly in terms of rates and selectivity of electrochemical CO_2 reduction. [EMMIm][BF_4] electrolytes almost exclusively facilitate the formation of CO. In contrast, [EM_4Im][BF_4] electrolytes produce a significant amount of formate in addition to CO. Meanwhile, [EM_4Im][BF_4] electrolytes yield a higher total current density compared to [EMMIm][BF_4] electrolytes at corresponding concentrations, which in turn leads to higher overall CO_2 reduction current density, meaning the combined partial current density of formate and CO formation, in [EM_4Im][BF_4] electrolytes (Fig. S4†).

Interestingly, the partial current density of formate in the electrolytes of all three ionic liquids always scales with that of H_2 and opposes that of CO (Fig. S2†). This trend strongly suggests that the formation of H_2 and formate share the same intermediate, which is most likely surface-adsorbed H (H*). Through bonding with either a proton or a CO_2 molecule from the electrolyte, H* will lead to the formation of H_2 or formate, respectively, as proposed by prior studies.[55,56] In contrast, surface adsorbed $CO_2^{\bullet-}$ leads to the formation of CO.

Notably, the comparison between total current densities from [EM_4Im][BF_4] and [EMMIm][BF_4] electrolytes show opposite results in chronoamperometry (Fig. 2) and voltammetry (Fig. 1). While higher total current densities are achieved in [EM_4Im][BF_4] electrolytes in chronoamperometry studies, [EMMIm][BF_4] electrolytes produce substantially higher current densities in voltammetry studies. This observation is consistent with further scan rate-dependent cyclic voltammetry analysis (Fig. S5†), which reveals significant mass transport limiting behaviors in [EMMIm][BF_4] electrolytes under CO_2 purging. This mass transport limit leads to a wave in the forward CV scan at low scan rates and causes the rapid drop of initial current density in chronoamperometry trials (Fig. S6†). [TBA][BF_4] and [EM_4Im][BF_4] electrolytes, however, did not show signs of mass transport limits in voltammetry (Fig. S7†), and the current density observed in voltammetry roughly matches that in chronoamperometry (Fig. S8†).

We hypothesize that such distinct behaviors in mass transport limitation and CO_2 reduction selectivity in [EM_4Im][BF_4] and [EMMIm][BF_4] electrolytes likely result from differences between the two imidazolium structures. Since a dense layer of cations is accumulated at electrochemical interfaces under the large cathodic applied potentials associated with CO_2 electrochemical reduction, the presence or absence of ring protons (C4/5-Hs) on imidazolium cations appears to cause drastically different local chemical environments, leading to different performances in CO_2 reduction.

We then performed further kinetic analysis to shed additional insight into the mechanism behind the structure–activity relationship of imidazolium cations in facilitating electrochemical CO_2 reduction. To achieve a consistent comparison, we conducted electrochemical CO_2 reduction in acetonitrile electrolytes of binary mixtures of [TBA][BF_4] and either [EM_4Im][BF_4] or [EMMIm][BF_4] by keeping a constant total ion concentration at 0.7 M. Controlling for a constant total ion concentration maintains consistent electrolyte conductivity (Fig. S9†) and relative concentration of proton donors, enabling a more unambiguous analysis of surface activities and reaction orders of different imidazolium cations, enabling more in-depth kinetic studies and analysis of electrochemical interfaces.

Fig. 3 shows the product selectivity in [TBA]/[EM_4Im][BF_4] and [TBA]/[EMMIm][BF_4] electrolytes with varying cation ratios at −2.5 V *vs.* Ag/Ag^+ under CO_2 purging over 1 hour CA. Importantly, both [EM_4Im]$^+$ and [EMMIm]$^+$ show strong surface activity by determining the product distribution at low relative concentrations, meaning that even low bulk concentrations of imidazolium cations are enough to sculpt an interfacial environment that mimics that of higher concentration electrolytes composed solely of imidazolium cations. In particular, increasing the imidazolium ionic liquid concentration from 0 to 0.025 M and 5 mM for [EM_4Im][BF_4] and [EMMIm][BF_4], respectively, is sufficient to switch the product selectivity from mainly H_2 to CO_2 reduction products. Further, the surface activity of [EMMIm]$^+$ is higher than that of [EM_4Im]$^+$, despite the fact that the [EM_4Im]$^+$ cation should be more weakly solvated due to the presence of additional bulky methyl groups in the place of ring hydrogens. Such trends of increased CO_2 reduction activity at increased relative imidazolium concentration at constant total ion concentrations also indicate the importance of having both adequate ionic strength and facilitating molecules to achieve efficient electrochemical CO_2 reduction.

Additionally, we find that the trend of reaction rates and product selectivity in binary mixture electrolytes are similar to single ionic liquid electrolytes. [TBA]/[EM_4Im][BF_4] electrolytes generally produce higher total current density and overall CO_2 reduction current density compared to [TBA]/[EMMIm][BF_4] (Fig. S10†). Additionally, [TBA]/[EM_4Im][BF_4] electrolytes produce an appreciable amount of both CO and formate, while [TBA]/[EMMIm][BF_4] almost exclusively catalyzes the formation of CO. Similar to [EMMIm][BF_4]-only electrolytes, [TBA]/[EMMIm][BF_4] electrolytes also exhibit mass transport limiting behaviors as the concentration of [EMMIm][BF_4] increases. CV scans in [TBA]/[EMMIm][BF_4] showed strong scan rate dependence once the concentration of [EMMIm][BF_4] exceeds 0.1 M (Fig. S11†). Apparent waves in forward scans and lower current density in reverse scans due to mass transport limits appear at lower scan rates (10 mV/s).

These mass transport limitations also cause the steady-state total current density in [TBA]/[EMMIm][BF_4] electrolytes to show a nonmonotonic dependence on [EMMIm][BF_4] concentration in CA studies (Fig. 3B). Increasing the concentration of [EMMIm][BF_4] from 0 to 0.025 M enhances the overall steady-state current density due to the facilitation of CO_2 reduction by [EMMIm]$^+$. However, further increasing the [EMMIm][BF_4] concentration invokes rapid drops of the initial CA current density (Fig. S12†), eventually leading to lower steady-state current densities at [EMMIm][BF_4] concentrations higher than 0.025 M. This trend of steady-state total current density is in stark contrast to that of [TBA]/[EM_4Im][BF_4] electrolytes, where the steady-state total current density monotonically increases with [EM_4Im][BF_4] concentration until saturation.

To better understand the origin of mass transport limitations and to enable further interpretation surrounding the structural uniqueness of [EMMIm]$^+$, we analyzed the reactions orders of CO_2 reduction to CO with respect to two main reactants, namely CO_2 and proton donor [Et_3NH]$^+$ (Fig. 4) in electrolytes consisting of 0.5 M [TBA][BF_4] and 0.2 M [EM_4Im][BF_4] ([TBA]$_{0.5}$/[EM_4Im]$_{0.2}$[BF_4]) or [EMMIm][BF_4] ([TBA]$_{0.5}$/[EMMIm]$_{0.2}$[BF_4]).

By keeping the [Et_3NH]Cl concentration constant at 0.05 M, the rate of CO formation exhibits a first-order dependence on the partial pressure of CO_2 in both [TBA]$_{0.5}$/[EM_4Im]$_{0.2}$[BF_4] and

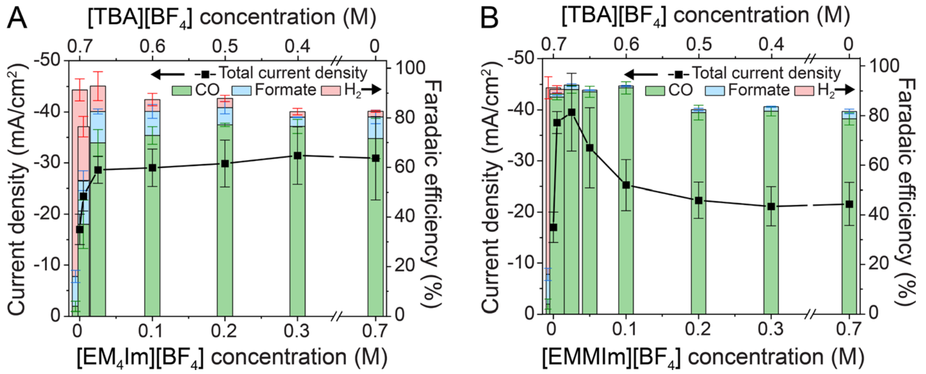

Fig. 3 Total current density and product selectivity of electrochemical CO_2 reduction in binary mixtures of (A) [EM_4Im][BF_4]/[TBA][BF_4] and (B) [EMMIm][BF_4]/[TBA][BF_4]. For each trial, the potential was held at −2.5 V *vs.* Ag/Ag^+ for 65 min under stirring (600 rpm) and CO_2 purging. The total concentration was constant at 0.7 M, and 0.05 M [Et_3NH]Cl was added to all electrolytes as the proton donor. Both [EM_4Im]$^+$ and [EMMIm]$^+$ show strong surface activity by defining the product selectivity at low concentrations (<0.05 M). Similar to single ionic liquid electrolytes, [EM_4Im][BF_4]/[TBA][BF_4] electrolytes generally facilitate higher steady-state current density and produce both formate and CO, while [EMMIm][BF_4]/[TBA][BF_4] electrolytes lead to lower steady-state current density but selectively produce CO.

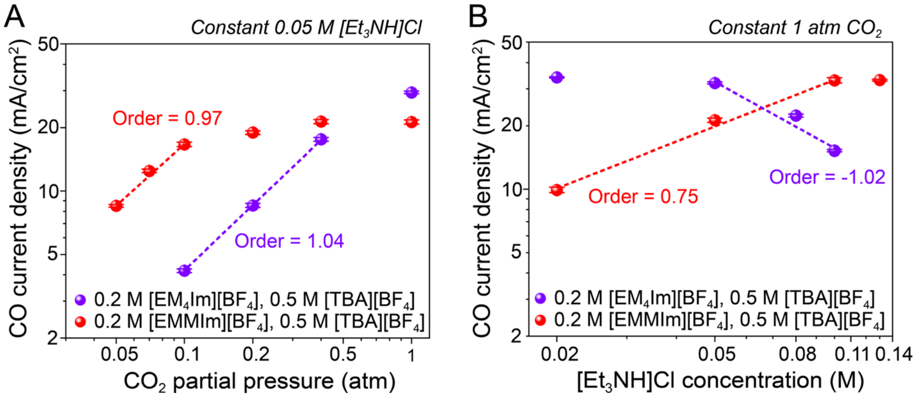

Fig. 4 Reaction orders of CO formation with respect to (A) CO_2 and (B) $[Et_3NH]^+$ in electrolytes consisting of 0.5 M [TBA][BF_4] and 0.2 M [EM_4Im][BF_4] (purple) or 0.2 M [EMMIm][BF_4] (red). For each trial, the potential was held at −2.5 V *vs.* Ag/Ag^+ for 11 min under stirring (600 rpm) and purging. (A) CO formation rate, characterized by CO partial current density, shows a first-order dependence on CO_2 partial pressure in both $[TBA]_{0.5}/[EM_4Im]_{0.2}[BF_4]$ and $[TBA]_{0.5}/[EMMIm]_{0.2}[BF_4]$. In $[TBA]_{0.5}/[EMMIm]_{0.2}[BF_4]$, the CO formation rate saturates at 0.1 atm CO_2 and achieves a maximum of around −20 mA cm^{-2}, indicating the existence of other factors limiting the rate of CO_2 reduction. In $[TBA]_{0.5}/[EM_4Im]_{0.2}[BF_4]$, the CO formation rate continuously increases with CO_2 partial pressure until 1 atm CO_2, where −30 mA cm^{-2} of CO formation is achieved. (B) The CO formation rate in $[TBA]_{0.5}/[EMMIm]_{0.2}[BF_4]$ positively depends on $[Et_3NH]^+$ concentration, suggesting the steady-state current is limited by the supply of protons. In $[TBA]_{0.5}/[EM_4Im]_{0.2}[BF_4]$, the CO formation rate is negatively related to $[Et_3NH]^+$ concentration, suggesting the competition for surface sites between H_2 formation and CO formation.

$[TBA]_{0.5}/[EMMIm]_{0.2}[BF_4]$ (Fig. 4A). Yet, the ranges of partial pressure where the first order dependence is observed are drastically different in the two electrolytes. In $[TBA]_{0.5}/[EM_4Im]_{0.2}[BF_4]$, an appreciable amount of CO formation occurs once the partial pressure of CO_2 exceeds 0.1 atm. The rate of CO formation shows a clean first-order dependence on the partial pressure of CO_2 up to 0.4 atm CO_2 and continues to increase until 1 atm of CO_2, where a partial current density of CO formation over −30 mA cm^{-2} is achieved.

In contrast, $[TBA]_{0.5}/[EMMIm]_{0.2}[BF_4]$ facilitates a considerable amount of CO formation when the CO_2 partial pressure is as low as 0.05 atm. The rate of CO formation shows a first-order dependence on CO_2 partial pressure in the range of 0.05 to 0.1 atm CO_2. Interestingly, the rate of CO formation saturates once the partial pressure of CO_2 exceeds 0.1 atm. Further increasing the CO_2 partial pressure only leads to minimal enhancement in CO formation, and the maximum CO formation rate achieved at 1 atm CO_2 is around −20 mA cm^{-2}, lower than that achieved in $[TBA]_{0.5}/[EM_4Im]_{0.2}[BF_4]$.

The earlier onset CO_2 partial pressure for CO formation in the $[TBA]_{0.5}/[EMMIm]_{0.2}[BF_4]$ demonstrates that the electrochemical interface defined by accumulated $[EMMIm]^+$ is more effective in capturing and facilitating the reduction of CO_2. More importantly, the saturation of CO formation at relatively low CO_2 partial pressure (0.1 atm) and lower maximum CO formation rate in $[TBA]_{0.5}/[EMMIm]_{0.2}[BF_4]$ strongly suggests that the accumulation of $[EMMIm]^+$ also introduces additional factors that limit CO_2 reduction, which is highly likely the transport of proton donors.

Analysis of the reaction order of CO formation with respect to proton donor, $[Et_3NH]Cl$, further unveils the unique regulation of transfer of $[Et_3NH]^+$ by accumulated $[EMMIm]^+$ (Fig. 4B). In $[TBA]_{0.5}/[EM_4Im]_{0.2}[BF_4]$ electrolytes, when the partial pressure of CO_2 is kept at 1 atm, increasing the $[Et_3NH]Cl$ concentration above 0.02 M leads to monotonic decrease in the CO formation rate and increase in the H_2 formation rate (Fig. S13†). A steep decrease in CO formation rate with a reaction order of −1 with respect to $[Et_3NH]Cl$ concentration occurs once the $[Et_3NH]Cl$ concentration is over 0.05 M. We attribute this negative $[Et_3NH]Cl$ reaction order to the competition of surface binding sites between hydrogen and $CO_2^{\bullet-}$ adsorption on Ag electrode surrounded by an $[EM_4Im]^+$-enriched chemical environment.

In $[TBA]_{0.5}/[EMMIm]_{0.2}[BF_4]$, the CO formation rate at 0.02 M $[Et_3NH]Cl$ is much lower than that in $[TBA]_{0.5}/[EM_4Im]_{0.2}[BF_4]$. However, increasing the $[Et_3NH]Cl$ concentration from 0.02 M to 0.1 M monotonically increases the CO formation rate, which is opposite to the trend observed in $[TBA]_{0.5}/[EM_4Im]_{0.2}[BF_4]$. This positive dependence of CO formation rate on $[Et_3NH]Cl$ concentration in $[TBA]_{0.5}/[EMMIm]_{0.2}[BF_4]$ indicates that under our standard conditions (1 atm CO_2, 0.05 M $[Et_3NH]Cl$), the supply of protons from $[Et_3NH]^+$ is the limiting factor for sustaining high steady-state CO_2 reduction rates.

More importantly, no significant competing formation of H_2 from direct reduction of $[Et_3NH]^+$ occurs in $[TBA]_{0.5}/[EMMIm]_{0.2}[BF_4]$ even in the presence of 0.1 M $[Et_3NH]Cl$ (Fig. S13†). The lack of H_2 formation strongly suggests that the formation of adsorbed hydrogen is unfavorable in $[EMMIm]^+$-containing electrolytes. Noticing that the formation of formate during CO_2 reduction was proposed to be initiated by surface-adsorbed hydrogen,[55,56] the unfavored formation of surface-adsorbed hydrogen would also explain the minimal selectivity towards formate production in $[EMMIm]^+$-containing electrolytes.

Taken together, we hypothesize that the distinct ability of $[EMMIm]^+$ to specifically promote CO_2 electrocatalytic reduction to CO is linked both to the presence of an aromatic imidazolium core that stabilizes the CO_2^- transition state *via* a π^+–anion interaction as well as a propensity to block surface access of the proton donor $[Et_3NH]^+$, which lowers the overall proton activity. These effects should simultaneously enhance the selectivity towards CO and limit the overall steady-state current density by depleting the proton donors at electrochemical interfaces, which is consistent with our measurements. To further evaluate this hypothesis on the influence of $[EMMIm]^+$-containing electrolytes, we conducted Tafel analysis on the electrochemical reduction of $[Et_3NH]^+$ to H_2 in electrolytes of three ionic liquids under Ar purging.

The electrochemical reduction of $[Et_3NH]^+$ to H_2 occurs through a two-step pathway:

Step 1:

$$Ag^* + [Et_3NH]^+ + e^- \rightleftharpoons Ag\text{-}H + Et_3N \quad \text{(Volmer step)}$$

Step 2:

$$Ag\text{-}H + [Et_3NH]^+ + e^- \rightleftharpoons H_2 + Et_3N + Ag^* \quad \text{(Heyrovsky step)}$$

Or:

$$2Ag\text{-}H \rightleftharpoons H_2 + 2Ag^* \quad \text{(Tafel step)}$$

Tafel plots are generated by plotting applied potential *versus* the rate of H_2 formation, represented by current density, on a logarithmic scale. Slopes in the linear region of Tafel plots provide mechanistic information, such as the identity of the rate-determining step (RDS) and the charge transfer coefficient if electron transfer is involved in the RDS. For instance, the Tafel slope of electrochemical H_2 formation with the first step (*i.e.*, Volmer step) as the RDS is predicted to be 120 mV/dec, assuming a charge transfer coefficient of 0.5.[57–59] When the second step becomes the RDS, much lower Tafel slopes (<40 mV/dec) are expected.[58,59]

Fig. 5 shows the Tafel plots of H_2 formation in 0.2 M $[TBA][BF_4]$, $[EM_4Im][BF_4]$, and $[EMMIm][BF_4]$ near the onset potential of H_2 formation. The overpotential required to drive the same H_2 formation rate in three electrolytes becomes more cathodic in the order of $[TBA][BF_4]$, $[EM_4Im][BF_4]$, and $[EMMIm][BF_4]$, suggesting the larger energy barrier of H_2 formation in 0.2 M $[EMMIm][BF_4]$.

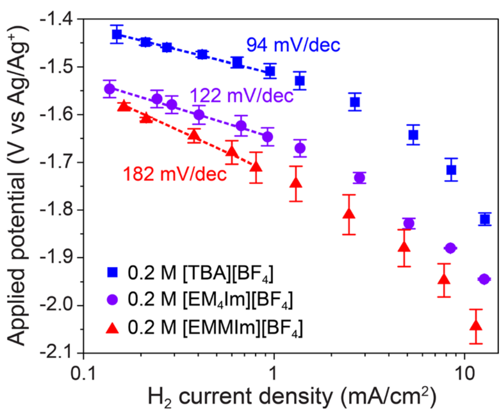

Fig. 5 Tafel plots of H_2 formation in 0.2 M $[TBA][BF_4]$ (blue), $[EM_4Im][BF_4]$ (purple), or $[EMMIm][BF_4]$ (red) electrolytes with 0.05 M $[Et_3NH]Cl$ under Ar purging. The slope from 0.2 M $[EMMIm][BF_4]$ in linear regime is much steeper than that from 0.2 M $[EM_4Im][BF_4]$ and 0.2 M $[TBA][BF_4]$, indicating the more sluggish kinetics of proton reduction and hydrogen adsorption in 0.2 M $[EMMIm][BF_4]$, likely due to the dense layer of potential driven assembly of $[EMMIm]^+$ on Ag electrode.

Further, the Tafel slope of H_2 formation in the linear region for 0.2 M $[EMMIm][BF_4]$ is 182 mV/dec, while the Tafel slopes in the linear region for 0.2 M $[TBA][BF_4]$ and $[EM_4Im][BF_4]$ are 94 mV/dec and 122 mV/dec, respectively. The Tafel slopes of H_2 formation in all three electrolytes are close to the characteristic Tafel slope of 120 mV/dec for pathways with the Vomer step as the RDS. However, the Tafel slope of 0.2 M $[EMMIm][BF_4]$ is much steeper than that of 0.2 M $[EM_4Im][BF_4]$ and $[TBA][BF_4]$, indicating a distinctively sluggish kinetics of the transfer of the first electron and the formation of surface adsorbed H (Ag-H) in 0.2 M $[EMMIm][BF_4]$.

The slower kinetics of Ag-H formation in 0.2 M $[EMMIm][BF_4]$ can result from either a limited mass transport of $[Et_3NH]^+$ in general, or a low charge transfer coefficient (<0.5) due to the hindered approach to the surface of proton centers caused by attracted $[EMMIm]^+$ layer. The latter scenario is analogous to the slow kinetics of H_2 formation in electrolytes with bulky proton donors.[60] It is also possible, and perhaps even likely, that two scenarios are simultaneously in effect. Further experiments that leverage rotating disc electrodes to explore a wider range of mass transport, applied bias, and current density regimes are necessary to fully determine the causes of slow H_2 formation kinetics in $[EMMIm][BF_4]$ electrolytes.

The more cathodic onset potential and the apparent slower kinetics of H_2 formation in the presence of $[EMMIm]^+$ are consistent with our conclusions surrounding the dual impact on electrochemical CO_2 reduction brought by the attracted $[EMMIm]^+$ layer on the Ag electrode. The unfavorable formation of Ag-H in the presence of $[EMMIm]^+$ layer ensures a high selectivity towards CO over H_2 and formate. However, the limited access of $[Et_3NH]^+$ to the electrode surface also compromises the steady-state rate of electrochemical CO_2 reduction due to the lack of an adequate proton supply to sustain proton-coupled electron transfers.

We propose that the unique regulation on Ag-H formation brought by $[EMMIm]^+$-containing electrolytes most likely originates from the assembly pattern of $[EMMIm]^+$ at electrochemical interfaces. The smaller H substituents at C4/5 positions of $[EMMIm]^+$ may lead to a denser assembly of $[EMMIm]^+$, thereby promoting the high surface activity of $[EMMIm]^+$ and giving rise to a physical barrier against the approach of $[Et_3NH]^+$. This scenario is analogous to the formation of hydrophobic layers and the suppression of water reduction caused by organic coating or ion assembly on electrode surfaces in aqueous systems.[25,61,62]

In contrast, the methyl groups at C4/5 positions of $[EM_4Im]^+$ cause steric hindrance for cation assembly, leading to a more loosely assembled layer of $[EM_4Im]^+$. Noticing that the interaction between imidazolium ring and adsorbed $CO_2^{\bullet-}$ is the key factor in driving CO_2 reduction, a denser assembly of $[EMMIm]^+$ would also explain the higher initial kinetics of CO_2 reduction reflected by CV studies at higher scan rates (Fig. 1).

In order to gain molecular insights into the behavior of bound cation layers at electrochemical interfaces, we investigated the electrochemical interfaces using the combination of surface-enhanced Raman scattering (SERS) and a molecular probe, namely 4-mercaptobenzonitrile (4-MBN). After being anchored on the Ag surface through the thiol group in the form of a self-assembled monolayer, the Raman shift of the nitrile group (–CN) provides information on local chemical environments around the electrochemical interfaces, mainly the strength of local electric fields that either destabilize (blue shift) or stabilize (redshift) the dipole of the probe molecule.[63,64]

Fig. 6 shows key SERS results of 4-MBN on a roughened Ag surface in 0.1 M [TBA][BF_4], [EM_4Im][BF_4], and [EMMIm][BF_4]. Full sets of potential-dependent SERS spectra of nitrile are included in the ESI (Fig. S14).† At open-circuit potential (OCP), all three cations drive redshifts of the nitrile group, indicating the stabilization of nitrile dipole in all three electrolytes. The significance of nitrile redshift increases in the sequence of $[TBA]^+$, $[EM_4Im]^+$, and $[EMMIm]^+$, with the redshifts driven by $[EM_4Im]^+$ and $[EMMIm]^+$ being closer to each other and much larger than that caused by $[TBA]^+$.

The dipole within the nitrile group points from the C atom (partially positive) to the N atom (partially negative). Therefore, the trend of nitrile Raman shift in three electrolytes indicates that the nitrile group experiences a stronger inward pointing local electric field (cathodic) and is more stabilized in two imidazolium-based electrolytes through the interaction with co-planar delocalized positive charges even at open-circuit potential. This trend suggests the preferential accumulation of imidazolium cations at electrochemical interfaces and explains their high surface activity illustrated in our CO_2 reduction results (Fig. 3).

To understand the behavior of three cations at electrochemical interfaces under cathodic applied potentials, we tracked the potential-dependent Raman shift of the nitrile group in 0.1 M [TBA][BF_4], [EM_4Im][BF_4], and [EMMIm][BF_4] under applied potentials ranging from −0.55 V to −0.90 V *vs.* Ag/Ag^+ (Fig. 6B). Importantly, the nitrile Raman shift in 0.1 M [EMMIm][BF_4] exhibits the largest redshift across the whole potential range among three electrolytes, indicating the strongest stabilization of nitrile by $[EMMIm]^+$. We further extracted the rate of change in nitrile Raman shift with respect to applied potentials (Fig. 6B and C), which is often referred to as the Stark tuning slope when the linear relationship holds. The Stark tuning slope reflects the sensitivity of the local electric field with respect to externally applied potentials as a result of ion rearrangements in electric double layers.

While the 0.1 M [TBA][BF_4] exhibits a constant Stark tuning slope of 7.3 cm^{-1}/V across the whole potential range, both 0.1 M [EM_4Im][BF_4] and 0.1 M [EMMIm][BF_4] show changing slopes depending on the applied potentials. Both imidazolium-based electrolytes give slopes slightly lower than that in 0.1 M [TBA][BF_4] in the potential range of −0.55 to −0.80 V *vs.* Ag/Ag^+, and steeper slopes in the potential range of −0.80 to −0.90 V *vs.* Ag/Ag^+. Interestingly, as shown in Fig. 6B and C, 0.1 M [EMMIm][BF_4] gives the lowest Stark tuning slope of 6.2 cm^{-1}/V under less cathodic applied potentials (−0.55 to −0.80 V *vs.* Ag/Ag^+) and the steepest slope of 10.2 cm^{-1}/V under more cathodic applied potentials (−0.80 to −0.90 V *vs.* Ag/Ag^+).

Similar potential-dependent changes in Stark tuning slopes were reported in [EMIm][BF_4] electrolytes, which was related to the structural transformation of the electric double layer containing $[EMIm]^+$ under more cathodic potentials.[65,66] We interpret such structural transformation as a result of the pre-ordering and potential-driven assembly of aromatic cations under cathodic potentials. The trend of nitrile Raman shift in three electrolytes at OCP suggests the preferential accumulation of imidazolium at electrochemical interfaces, which means that the surface potential of the electrode could be better screened or even overscreened at OCP, which was previously reported for several ionic liquid electrolytes.[67–69] Therefore, less ion rearrangement is required in imidazolium-containing electrolytes

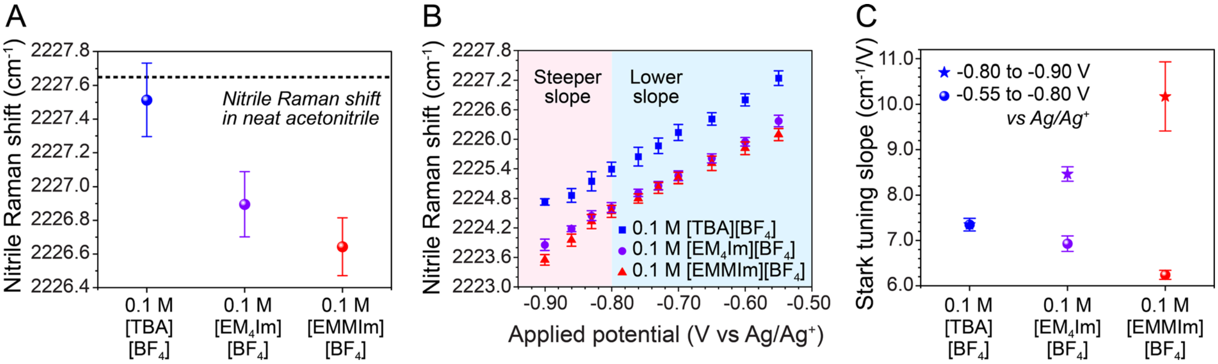

Fig. 6 Raman shifts of the nitrile group from 4-MBN in 0.1 M [TBA][BF_4] (blue), [EM_4Im][BF_4] (purple), and [EMMIm][BF_4] (red). (A) Raman shifts of the nitrile group at OCP in three electrolytes. The nitrile group exhibits redshifts in all three electrolytes. The redshifts are more significant in the two imidazolium-based electrolytes, indicating the stronger stabilization of the nitrile dipole by imidazolium. (B) Potential-dependent Raman shifts of the nitrile group in the three electrolytes. Larger redshifts of the nitrile group are observed in both imidazolium-based electrolytes across the whole potential range tested, suggesting that the potential-driven assembly of imidazolium gives rise to a stronger interfacial electric field that stabilizes the nitrile dipole. Further, two distinct Stark tuning slopes were observed for both imidazolium-based electrolytes in different potential ranges. (C) Potential-dependent Stark tuning slopes in three electrolytes. Compared to 0.2 M [TBA][BF_4], both 0.2 M [EM_4Im][BF_4] and [EMMIm][BF_4] exhibit lower slopes under less cathodic applied potentials and steeper slope under more cathodic applied potentials, suggesting the ordered pre-assembly and more efficient potential-driven assembly of imidazolium in two potential ranges, respectively.

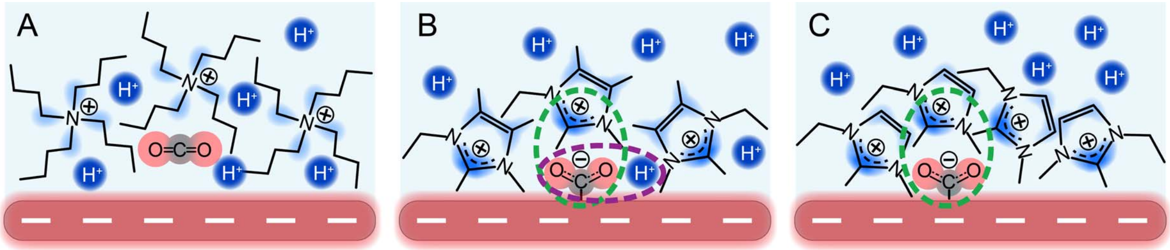

$[TBA]^+$
Inactive CO_2 reduction
Active H_2 formation

$[EM_4Im]^+$:
High overall CO_2 reduction rate
Mixed products

$[EMMIm]^+$:
Low overall CO_2 reduction rate
High CO selectivity

Fig. 7 Imidazolium cations promote and regulate CO_2 reduction. The interaction between co-planar delocalized positive charge in imidazolium and anionic intermediate $CO_2^{\bullet-}$ (dashed green circle) is the most essential to promote CO_2 reduction. (A) Without the co-planar delocalized positive charge, $[TBA]^+$ cannot effetively stabilize CO_2, and H_2 becomes the main product from the direction reduction of $[Et_3NH]^+$. In contrast, both (B) $[EM_4Im]^+$ and (C) $[EMMIm]^+$ can facilitate efficient CO_2 reduction. However, a steady supply of protons is necessary to complete electron transfer and to sustain the current (dashed purple circle). Therefore, (C) $[EMMIm]^+$ that exhibits a more ordered assembly at the interface limits the supply of proton, which compromises the steady-state current density.

under less cathodic applied potentials, leading to lower sensitivity of the interfacial electric field to applied potentials and lower Stark tuning slopes.

However, once the applied potential exceeds the screening capability of bound cations, the rearrangement of ions within the electric double layer becomes necessary to fully screen the surface potential of electrodes. In this case, cations that can be more easily assembled at OCP will also more efficiently rearrange and screen the surface potential, leading to steeper Stark tuning slopes. Therefore, the steepest Stark tuning slope in 0.1 M $[EMMIm][BF_4]$ at more cathodic applied potentials illustrates the most efficient potential-driven assembly of $[EMMIm]^+$ and the strongest stabilization of nitrile. The relatively lower Stark tuning slope of 0.1 M $[EM_4Im][BF_4]$ suggests the moderate assembly efficiency and nitrile stabilization of $[EM_4Im]^+$. In contrast to the two imidazolium-based electrolytes, 0.1 M $[TBA][BF_4]$, with the potential-independent Stark tuning slope and the lowest Stark tuning slope under more cathodic applied potentials, exhibits the lowest assembly efficiency and stabilization of nitrile groups.

Overall, the trends of OCP nitrile Raman shift position and potential-dependent Stark tuning rate in 0.1 M $[TBA][BF_4]$, $[EM_4Im][BF_4]$, and $[EMMIm][BF_4]$ illustrate that imidazolium with co-planarly delocalized positive charges generally exhibit higher assembly efficiency and better stabilize nitrile by interfacial electric field across the whole range of applied potentials. Although the monolayer of 4-MBN cannot directly probe interfacial properties at more cathodic applied potentials due to 4-MBN desorption, an extrapolation of nitrile Raman shift using the Stark tuning slopes for more cathodic applied potentials implies the even higher interfacial electric field brought by accumulated $[EMMIm]^+$ and $[EM_4Im]^+$ at applied potentials applicable for electrochemical CO_2 reduction.

Imidazolium cations are known to collectively reorientate to parallel alignment with respect to the electrode surface under cathodic applied potentials.[44,70,71] Such reorientation aligns imidazolium cations with each other and reduces the average distance between the imidazolium charge center and electrode surface, which together may contribute to the efficient assembly of imidazolium and better stabilization of surface adsorbed molecules under cathodic applied potentials. Particularly, $[EMMIm]^+$, with smaller ring substituents, would undergo the reorientation more easily and exhibit more ordered assembly compared to $[EM_4Im]^+$, leading to stronger interfacial electric fields.

The trends of the structure-dependent cation assembly and interfacial electric field under cathodic applied potentials are expected to be further relevant under conditions for CO_2 reduction. Adsorbed $CO_2^{\bullet-}$ possesses an overall molecular dipole along the same direction as the nitrile group, so the trend of nitrile stabilization by cations should also be consistent with the trends of the relative stabilization of the $CO_2^{\bullet-}$ transition state. Therefore, instant CO_2 reduction kinetics is predicted to increase in the order of $[TBA][BF_4]$, $[EM_4Im][BF_4]$, and $[EMMIm][BF_4]$, which corresponds well to our CV results (Fig. 1). At the same time, the particularly dense and ordered assembly of $[EMMIm]^+$ also hinders the transport of proton donors and the adsorption of hydrogen, leading to slower H_2 transfer kinetics and compromised steady-state CO_2 reduction rate that depends on the supply of protons (Fig. 7).

Conclusion

By comparing electrochemical CO_2 reduction in $[EM_4Im]^+$ and $[EMMIm]^+$-based electrolytes in the presence of independent organic proton donor, we successfully decoupled the different contributions of imidazolium promoters to CO_2 electrocatalytic reduction. Our data demonstrates that the co-planarly delocalized positive charge on imidazolium rings is the key moiety to enabling imidazolium cations to stabilize adsorbed $CO_2^{\bullet-}$. Further, our results of [TBA]/imidazolium mixtures indicates that the ring structure of imidazolium cations enhances their surface activity, eventually promoting selective CO_2 reduction even at relatively low bulk concentrations.

Drawing on kinetic and surface-enhanced spectroscopic studies, we illustrate that the size and identity of aromatic substituents of $[EMMIm]^+$ enables it to densely assemble on cathode surfaces. This blocking bound ion layer appears to modify the local chemical environment to hinder the access of proton donors, which suppresses proton activity, relative to that of CO_2 reduction. In particular, $[EMMIm]^+$ exhibits uniquely high surface activity, high kinetic current density at a short time scale, and distinct enhancement of CO selectivity during CO_2 reduction. The dense assembly of $[EMMIm]^+$, however, also compromises the steady-state current density of CO_2 reduction due to suppressing proton activity to the point where there is a deficiency of active species needed to sustain proton-coupled electron transfers involved in CO_2 reduction. Therefore, $[EM_4Im]^+$, with a bulkier structure and moderated assembly density, provides the optimum performance during steady-state CO_2 reduction.

Overall, our findings yield new insights into how the imidazolium core and surrounding ring substituents influence electrochemical CO_2. Our study raises the prospect that aromatic cations have distinct interfacial assembly and intermolecular interactions with anionic intermediates *via* a "π^+–anion" interaction that appears to be an electrostatic analog of the more commonly investigated "cation–π" interaction.[53,54] Furthermore, our study suggests new criteria for designing electrolytes that balance the suppression of H_2 formation and the support of proton-coupled electron transfer, which is especially critical for facilitating selective yet fast CO_2 reduction.

Data availability

The data supporting this article have been included as part of the main text and ESI.†

Author contribution

Wenxiao Guo: conceptualization (lead, equal); methodology (lead); investigation (lead); formal analysis (lead, equal); writing – original draft (lead); writing – review and editing (equal). Beichen Liu: conceptualization (supporting); methodology (supporting); writing – review and editing (equal). Seth Anderson: methodology (supporting); investigation (supporting); formal analysis (supporting); writing – review and editing (equal). Samuel Johnstone: methodology (supporting); writing – review and editing (equal). Matthew Gebbie: conceptualization (lead, equal); methodology (supporting); formal analysis (lead, equal); writing – review and editing (equal); supervision (lead); funding acquisition (lead).

Conflicts of interest

There are no conflicts to declare.

Acknowledgements

This material is based upon work supported by the National Science Foundation under Award No. 2237311. Acknowledgement is made to the donors of the American Chemical Society Petroleum Research Fund for partial support of this reasearch. M. A. G. acknowledges support from the Michael F. and Virginia H. Conway Assistant Professorship. B. L. acknowledges support from the Fenton-May Graduate Fellowship. The authors gratefully acknowledge use of facilities and instrumentation at the UW-Madison Wisconsin Centers for Nanoscale Technology (**https://wcnt.wisc.edu/**) partially supported by the NSF through the University of Wisconsin Materials Research Science and Engineering Center (DMR-2309000). The Bruker Avance III 400 NMR spectrometer was supported by NSF grant CHE-1048642. We extend our gratitude to Prof. Whitney Loo and her group for their assistance with the use of BioLogic VSP 3e potentiostat and the measurement of EIS data.

References

1 I. Sullivan, A. Goryachev, I. A. Digdaya, X. Li, H. A. Atwater, D. A. Vermaas and C. Xiang, *Nat. Catal.*, 2021, **4**, 952–958.

2 X. She, L. Zhai, Y. Wang, P. Xiong, M. M.-J. Li, T.-S. Wu, M. C. Wong, X. Guo, Z. Xu, H. Li, H. Xu, Y. Zhu, S. C. E. Tsang and S. P. Lau, *Nat. Energy*, 2024, **9**, 81–91.

3 H. Wu, L. Huang, J. Timoshenko, K. Qi, W. Wang, J. Liu, Y. Zhang, S. Yang, E. Petit, V. Flaud, J. Li, C. Salameh, P. Miele, L. Lajaunie, B. Roldán Cuenya, D. Rao and D. Voiry, *Nat. Energy*, 2024, **9**, 422–433.

4 M. Ramdin, B. De Mot, A. R. T. Morrison, T. Breugelmans, L. J. P. van den Broeke, J. P. M. Trusler, R. Kortlever, W. de Jong, O. A. Moultos, P. Xiao, P. A. Webley and T. J. H. Vlugt, *Ind. Eng. Chem. Res.*, 2021, **60**, 17862–17880.

5 H. Shin, K. U. Hansen and F. Jiao, *Nat Sustainability*, 2021, **4**, 911–919.

6 H. Cao, Z. Zhang, J.-W. Chen and Y.-G. Wang, *ACS Catal.*, 2022, **12**, 6606–6617.

7 X. Liu, J. Xiao, H. Peng, X. Hong, K. Chan and J. K. Norskov, *Nat. Commun.*, 2017, **8**, 15438.

8 L. Guo, J. Zhou, F. Liu, X. Meng, Y. Ma, F. Hao, Y. Xiong and Z. Fan, *ACS Nano*, 2024, **18**, 9823–9851.

9 Y. Zhao, X. Liu, J. Chen, J. Chen, J. Chen, L. Fan, H. Yang, S. Xi, L. Shen and L. Wang, *Proc. Natl. Acad. Sci. U. S. A.*, 2023, **120**, e2218040120.

10 Y. Yang, S. Louisia, S. Yu, J. Jin, I. Roh, C. Chen, M. V. Fonseca Guzman, J. Feijoo, P. C. Chen, H. Wang, C. J. Pollock, X. Huang, Y. T. Shao, C. Wang, D. A. Muller, H. D. Abruna and P. Yang, *Nature*, 2023, **614**, 262–269.

11 H. Yun, W. Choi, D. Shin, H.-S. Oh and Y. J. Hwang, *ACS Catal.*, 2023, **13**, 9302–9312.

12 T. Zheng, C. Liu, C. Guo, M. Zhang, X. Li, Q. Jiang, W. Xue, H. Li, A. Li, C. W. Pao, J. Xiao, C. Xia and J. Zeng, *Nat. Nanotechnol.*, 2021, **16**, 1386–1393.

13 M. Yang, J. Wu, Y. Li, H. Pan, H. Cui, X. Lu and X. Tang, *ACS Catal.*, 2024, **14**, 6169–6178.

14 Z. H. Zhao, J. R. Huang, P. Q. Liao and X. M. Chen, *Angew Chem. Int. Ed. Engl.*, 2023, **62**, e202301767.

15 S. Osella and W. A. Goddard III, *J. Am. Chem. Soc.*, 2023, **145**, 21319–21329.

16 S. Feng, X. Wang, D. Cheng, Y. Luo, M. Shen, J. Wang, W. Zhao, S. Fang, H. Zheng, L. Ji, X. Zhang, W. Xu,

Y. Liang, P. Sautet and J. Zhu, *Angew Chem. Int. Ed. Engl.*, 2024, **63**, e202317942.

17 X. Zhong, H.-J. Peng, C. Xia and X. Liu, *J. Phys. Chem. C*, 2024, **128**, 3621–3631.

18 M. A. Gebbie, B. Liu, W. Guo, S. R. Anderson and S. G. Johnstone, *ACS Catal.*, 2023, **13**, 16222–16239.

19 Z. Zheng, Y. Yao, W. Yan, H. Bu, J. Huang and M. Ma, *ACS Catal.*, 2024, **14**, 6328–6338.

20 G. Kastlunger, L. Wang, N. Govindarajan, H. H. Heenen, S. Ringe, T. Jaramillo, C. Hahn and K. Chan, *ACS Catal.*, 2022, **12**, 4344–4357.

21 S. Vijay, W. Ju, S. Brückner, S.-C. Tsang, P. Strasser and K. Chan, *Nat. Catal.*, 2021, **4**, 1024–1031.

22 N. Govindarajan, A. Xu and K. Chan, *Science*, 2022, **375**, 379–380.

23 M. C. O. Monteiro, M. F. Philips, K. J. P. Schouten and M. T. M. Koper, *Nat. Commun.*, 2021, **12**, 4943.

24 S. Ringe, E. L. Clark, J. Resasco, A. Walton, B. Seger, A. T. Bell and K. Chan, *Energy Environ. Sci.*, 2019, **12**, 3001–3014.

25 X. Yang, H. Ding, S. Li, S. Zheng, J. F. Li and F. Pan, *J. Am. Chem. Soc.*, 2024, **146**, 5532–5542.

26 M. C. O. Monteiro, F. Dattila, B. Hagedoorn, R. García-Muelas, N. López and M. T. M. Koper, *Nat. Catal.*, 2021, **4**, 654–662.

27 H. Zhang, J. Gao, D. Raciti and A. S. Hall, *Nat. Catal.*, 2023, **6**, 807–817.

28 J. Gu, S. Liu, W. Ni, W. Ren, S. Haussener and X. Hu, *Nat. Catal.*, 2022, **5**, 268–276.

29 W. Ren, A. Xu, K. Chan and X. Hu, *Angew Chem. Int. Ed. Engl.*, 2022, **61**, e202214173.

30 S. Dongare, O. K. Coskun, E. Cagli, J. S. Stanley, A. Q. Mir, R. S. Brower, J. M. Velazquez, J. Y. Yang, R. L. Sacci and B. Gurkan, *Langmuir*, 2024, **40**, 9426–9438.

31 O. K. Coskun, S. Dongare, B. Doherty, A. Klemm, M. Tuckerman and B. Gurkan, *Angew Chem. Int. Ed. Engl.*, 2024, **63**, e202312163.

32 N. R. Pitawela and S. K. Shaw, *ACS Meas. Sci. Au*, 2021, **1**, 117–130.

33 V. V. Chaban, I. V. Voroshylova, O. N. Kalugin and O. V. Prezhdo, *J. Phys. Chem. B*, 2012, **116**, 7719–7727.

34 B. Ratschmeier, C. Paulsen, K. Stallberg, G. Roß, W. Daum, R. Pöttgen and B. Braunschweig, *ACS Catal.*, 2024, **14**, 1773–1784.

35 T. Kunene, A. Atifi and J. Rosenthal, *ACS Appl. Energy Mater.*, 2019, **3**, 4193–4200.

36 J. Yang, X. Kang, J. Jiao, X. Xing, Y. Yin, S. Jia, M. Chu, S. Han, W. Xia, H. Wu, M. He and B. Han, *J. Am. Chem. Soc.*, 2023, **145**, 11512–11517.

37 B. A. Rosen, A. Salehi-Khojin, M. R. Thorson, W. Zhu, D. T. Whipple, P. J. Kenis and R. I. Masel, *Science*, 2011, **334**, 643–644.

38 B. Liu, W. Guo and M. A. Gebbie, *ACS Catal.*, 2022, **12**, 9706–9716.

39 S. Noh, Y. J. Cho, G. Zhang and M. Schreier, *J. Am. Chem. Soc.*, 2023, **145**, 27657–27663.

40 G. P. Lau, M. Schreier, D. Vasilyev, R. Scopelliti, M. Gratzel and P. J. Dyson, *J. Am. Chem. Soc.*, 2016, **138**, 7820–7823.

41 K. Motobayashi, Y. Maeno and K. Ikeda, *J. Phys. Chem. C*, 2022, **126**, 11981–11986.

42 Z. Min, B. Chang, C. Shao, X. Su, N. Wang, Z. Li, H. Wang, Y. Zhao, M. Fan and J. Wang, *Appl. Catal., B*, 2023, **326**, 122185.

43 S. Neyrizi, J. Kiewiet, M. A. Hempenius and G. Mul, *ACS Energy Lett.*, 2022, **7**, 3439–3446.

44 W. Guo, B. Liu and M. A. Gebbie, *J. Phys. Chem. C*, 2023, **127**, 14243–14254.

45 B. Ratschmeier and B. Braunschweig, *J. Phys. Chem. C*, 2021, **125**, 16498–16507.

46 D. V. Vasilyev, S. Shyshkanov, E. Shirzadi, S. A. Katsyuba, M. K. Nazeeruddin and P. J. Dyson, *ACS Appl. Energy Mater.*, 2020, **3**, 4690–4698.

47 B. C. Kash, R. J. Gomes and C. V. Amanchukwu, *J. Phys. Chem. Lett.*, 2023, **14**, 920–926.

48 A. J. Fry, *J. Org. Chem.*, 2015, **80**, 3758–3765.

49 Y. Wang and G. Tian, *Langmuir*, 2023, **39**, 14231–14245.

50 P. A. Hunt, *J. Phys. Chem. B*, 2007, **111**, 4844–4853.

51 J. A. Fournier, C. T. Wolke, C. J. Johnson, A. B. McCoy and M. A. Johnson, *J. Chem. Phys.*, 2015, **142**, 064306.

52 T. Endo, T. Kato and K. Nishikawa, *J. Phys. Chem. B*, 2010, **114**, 9201–9208.

53 M. A. Gebbie, W. Wei, A. M. Schrader, T. R. Cristiani, H. A. Dobbs, M. Idso, B. F. Chmelka, J. H. Waite and J. N. Israelachvili, *Nat. Chem.*, 2017, **9**, 473–479.

54 J. P. Gallivan and D. A. Dougherty, *Proc. Natl. Acad. Sci. U. S. A.*, 1999, **96**, 9459–9464.

55 X. Guo, S.-M. Xu, H. Zhou, Y. Ren, R. Ge, M. Xu, L. Zheng, X. Kong, M. Shao, Z. Li and H. Duan, *ACS Catal.*, 2022, **12**, 10551–10559.

56 D. Bohra, I. Ledezma-Yanez, G. Li, W. de Jong, E. A. Pidko and W. A. Smith, *Angew Chem. Int. Ed. Engl.*, 2019, **58**, 1345–1349.

57 O. van der Heijden, S. Park, R. E. Vos, J. J. J. Eggebeen and M. T. M. Koper, *ACS Energy Lett.*, 2024, **9**, 1871–1879.

58 T. Shinagawa, A. T. Garcia-Esparza and K. Takanabe, *Sci. Rep.*, 2015, **5**, 13801.

59 J. Zhu, L. Hu, P. Zhao, L. Y. S. Lee and K. Y. Wong, *Chem. Rev.*, 2020, **120**, 851–918.

60 M. N. Jackson and Y. Surendranath, *J. Am. Chem. Soc.*, 2016, **138**, 3228–3234.

61 N. B. Watkins, Y. Wu, W. Nie, J. C. Peters and T. Agapie, *ACS Energy Lett.*, 2022, **8**, 189–195.

62 A. K. Pennathur, C. Tseng, N. Salazar and J. M. Dawlaty, *J. Am. Chem. Soc.*, 2023, **145**, 2421–2429.

63 S. Sarkar, A. Maitra, S. Banerjee, V. S. Thoi and J. M. Dawlaty, *J. Phys. Chem. B*, 2020, **124**, 1311–1321.

64 S. Sarkar, A. Maitra, W. R. Lake, R. E. Warburton, S. Hammes-Schiffer and J. M. Dawlaty, *J. Am. Chem. Soc.*, 2021, **143**, 8381–8390.

65 N. Garcia Rey and D. D. Dlott, *Phys. Chem. Chem. Phys.*, 2017, **19**, 10491–10501.

66 N. García Rey and D. D. Dlott, *J. Phys. Chem. C*, 2015, **119**, 20892–20899.

67 M. Z. Bazant, B. D. Storey and A. A. Kornyshev, *Phys. Rev. Lett.*, 2011, **106**, 046102.

68 J. P. de Souza and M. Z. Bazant, *J. Phys. Chem. C*, 2020, **124**, 11414–11421.
69 A. M. Smith, K. R. Lovelock and S. Perkin, *Faraday Discuss.*, 2013, **167**, 279–292.
70 B. Liu, W. Guo, S. R. Anderson, S. G. Johnstone, S. Wu, M. C. Herrington and M. A. Gebbie, *Soft Matter*, 2024, **20**, 351–364.
71 M. Zhang, S. Duan, S. Luo, Y. Zhong, J. Yan, G. Liu, B. Mao and Z. Tian, *ChemElectroChem*, 2020, **7**, 4936–4942.